Low-frequency Oscillations and Resonance Analysis of VSG-controlled PMSG-based Wind Generation Systems

Yizhuo Ma, *Graduate Student Member*, *IEEE*, Jin Xu, Chenxiang Gao, *Student Member*, *IEEE*, Guojie Li, *Senior Member*, *IEEE*, and Keyou Wang, *Member*, *IEEE*

***Abstract*—With good adaptability to weak power grids, the grid-forming inverter becomes the foundation of future power grids with high-proportion renewable energy. Moreover, the virtual synchronous generator (VSG) control is recognized as the mainstream control strategy for grid-forming inverters. For permanent magnet synchronous generator (PMSG) based wind generation systems connected to power grid via VSG-controlled grid-forming inverters, some novel impacts on the low-frequency oscillations (LFOs) emerge in power grids. The first impact involves the negative/positive damping effect on LFOs. In this paper, the small-signal torque model of VSG-controlled PMSG-based wind generation systems is established based on the damping torque analysis method, revealing the influence mechanism of machine-side dynamics on LFOs and proving the necessity of the double-mass model for accurate stability analysis. The second impact is the resonance effect between torsional oscillation and LFOs. Subsequently, this paper uses the open-loop resonance analysis method to study the resonance mechanism and to predict the root trajectory. Then, a damping enhancement strategy is proposed to weaken and eliminate the negative damping effect of machine-side dynamics on LFOs and the resonance effect between torsional oscillation and LFOs. Finally, the analysis result is validated through a case study involving the connection of the VSG-controlled PMSG-based wind generation system to the IEEE 39-bus AC grid, supporting the industrial application and stable operation of VSG-controlled PMSG-based wind generation systems.**

***Index Terms*—Grid-forming inverter, low-frequency oscillation (LFO), modal resonance, permanent magnet synchronous generator (PMSG), torsional oscillation, virtual synchronous generator (VSG).**

I. Introduction

In recent years, the global initiative to achieve carbon neutrality has accelerated the development of renewable energy, leading to a rapid increase in its penetration rate [1]. Currently, most renewable energy systems utilize grid-following control, which is inadequate for meeting the requirements of grid frequency, inertia, and voltage support as the renewable energy penetration increases [2]. Therefore, there is a need to enhance the active support capability of renewable energy. The renewable energy systems with grid-forming inverters controlled by virtual synchronous generator (VSG) can simulate voltage source characteristics while supporting voltage and frequency. In the future, it is crucial to gradually increase the deployment of VSG-controlled renewable energy systems for stable operation in weak grids [3], [4]. However, the VSG-controlled renewable energy systems may encounter low-frequency oscillations (LFOs) similar to synchronous generators (SGs) when simulating rotor dynamics on the grid side. Unlike SGs, the behavior of LFOs in VSG-controlled renewable energy systems is more complex and primarily related to control sections. The research in this field is still in progress and requires further refinement [5], [6].

Most research on the stability of VSG-controlled systems under LFOs focuses on grid-connected inverters employing the constant DC-link voltage control [7]-[12]. Reference [7] investigates the influence mechanism of VSG-controlled voltage source converters (VSCs) on LFOs using damping torque analysis method and identifies that the introduction of phase-locked loops (PLLs) can exert a negative damping effect on LFOs. References [8] and [9] establish small-signal state-space models for VSG-controlled inverters considering outer voltage loops, where it can be observed that increasing the virtual impedance and active damping coefficient is advantageous for enhancing the stability in low-frequency range. Reference [10] examines the LFOs in a system comprising grid-following and grid-forming VSCs and finds that the damping coefficients and the proportional coefficient of the proportional-integral (PI) controller of PLL primarily influence the damping of LFOs. In [11], a small-signal model of VSG considering the governor is developed to investigate the influence mechanism of VSG on inter-area LFOs based on the participation factor analysis, elucidating the influence

Manuscript received: May 4, 2024; revised: July 9, 2024; accepted: September 3, 2024. Date of CrossCheck: September 3, 2024. Date of online publication: October 24, 2024.

This work was supported in part by the National Key R&D Program of China (No. 2022YFE0105200) and in part by the State Grid Zhejiang Electric Power Company Science and Technology Program (No. 5211JX230004).

This article is distributed under the terms of the Creative Commons Attribution 4.0 International License (http://creativecommons.org/licenses/by/4.0/).

Y. Ma (corresponding author), J. Xu, C. Gao, G. Li, and K. Wang are with the Key Laboratory of Control of Power Transmission and Conversion Ministry of Education, Shanghai Jiao Tong University, Shanghai, China (e-mail: 925998709@sjtu.edu.cn; xujin20506@sjtu.edu.cn; gaocx_22@sjtu.edu.cn; liguojie@sjtu.edu.cn; wangkeyou@sjtu.edu.cn)

DOI: 10.35833/MPCE.2024.000465

patterns of various parameters. Reference [12] suggests an active damping approach for multiple grid-connected VSGs in power grid to mitigate LFOs. There is limited research on the impact of VSG-controlled renewable energy resource such as permanent magnet synchronous generator (PMSG) on the system stability under LFOs.

The PMSG-based wind generation systems have rapidly evolved and emerged as a prominent power source. Besides, the VSG control is one of the mainstream grid-forming control methods [13]. In this method, the DC-link voltage is regulated in the machine-side control (MSC) section, and the active power is controlled via the maximum power point tracking (MPPT), while the rotor motion equation of SGs is simulated in the grid-side control (GSC) section. The VSG control harnesses the kinetic energy stored in the wind turbine (WT) rotor to provide the voltage/frequency support to power grids. This control method inevitably causes the machine-side dynamics of PMSG to affect LFOs in power systems through the MPPT on the GSC.

Only a few studies have explored the impact of integrating VSG-controlled PMSG-based wind generation systems on LFOs in power systems [14]-[17]. Reference [14] analyzes the small-signal stability of a VSG-controlled PMSG-based wind farm (WF) under weak grid conditions. This study illustrates that WFs equipped with VSGs remain stable even under weak grid conditions, with VSG parameters posing no risk of instability. References [15] and 16] investigate the influence of WT dynamics on the stability of grid-connected wind generation systems using VSG control through the damping torque analysis method. However, this study makes several simplifications and does not quantitatively demonstrate the damping effect of machine-side dynamics on LFOs. Reference [17] introduces a unified damping torque model for PMSG, indicating that the negative damping torque generated by the drive train is the primary cause of LFOs in WTs. Besides, [17] makes a simplification by adopting the single-mass model to describe the shaft system dynamics. However, due to the flexibility of shaft systems in PMSG-based wind generation systems, the double-mass model should be employed in the shaft system, which will inevitably introduce more complex stability issues than using the single-mass model.

Furthermore, the flexible shaft system in PMSG-based wind generation systems induces torsional oscillation within the frequency range of 0.1-10 Hz [18], while LFOs in power systems typically occur within 0.1-2 Hz [12]. Under the VSG control, the coupling arises between machine-side and grid-side dynamics due to the alignment of torsional oscillation frequency with that of LFOs. Consequently, the resonance effects between torsional oscillation and LFOs may arise, presenting potential risks to system stability. References [19] - [21] discuss the dynamic interactions between PMSG-based wind generation systems and power system using the open-loop resonance analysis method, which considers the closed-loop system as a combination of two open-loop subsystems. The resonance occurs when the two open-loop subsystems approach with each other on the complex plane. This method accurately computes the damping of oscillation modes during resonance and can determine whether the system is stable. Therefore, this method offers an advantage for addressing potential resonance between torsional oscillation and LFOs.

To fill the identified research gap, this paper develops a small-signal torque model for VSG-controlled PMSG-based wind generation systems, incorporating machine-side dynamics using the double-mass model, as well as considering the DC-link and grid-side dynamics based on the damping torque analysis method. Then, this paper elucidates the influence mechanism of machine-side dynamics on LFOs and compares the effects of single-mass and double-mass models on LFOs, demonstrating the necessity of the double-mass model for precise stability analysis and enabling the quantitative assessment of damping effects of each torque component on LFOs. Subsequently, this paper employs the open-loop resonance analysis method to examine the resonance mechanism between torsional oscillations and LFOs, and utilizes the residue method to predict the root locus accurately. Then, a damping enhancement strategy is proposed to weaken and eliminate the negative damping effect of machine-side dynamics and resonance. Finally, a time-domain simulation model for VSG-controlled PMSG-based wind generation systems connected to the IEEE 39-bus AC grid is developed in MATLAB/Simulink to validate the accuracy of theoretical analysis and the effectiveness of the proposed damping enhancement strategy.

The remainder of this paper is structured as follows. Section II discusses the modeling and control of VSG-controlled PMSG-based wind generation systems. Section III examines the damping effect of machine-side dynamics of PMSG on LFOs and the resonance effect between torsional oscillation and LFOs, and presents a damping enhancement strategy. Section IV presents the time-domain simulation results. Finally, Section V provides the conclusions.

II. Modeling and Control of VSG-controlled PMSG-based Wind Generation Systems

The typical topology of the VSG-controlled PMSG-based wind generation system, as depicted in Fig. 1, comprises various components: WT, shaft system, PMSG, back-to-back full-power converter, transformers, GSC control section, MSC control section, LCL filter, and grid-connected line. This section introduces a mathematical model of the studied system in Fig. 1 using the per-unit system, where PWM is short for pulse width modulation.

A. PMSG Model

The PMSG is controlled in *dq* rotating coordinates, aligning the *d*-axis with the magnetic flux linkage of the rotor ψ_f. The stator voltage is expressed as [22]:

$$\begin{cases} u_{sd} = -R_s i_{sd} - \dfrac{L_d}{\omega_{eb}} \dfrac{\mathrm{d}i_{sd}}{\mathrm{d}t} + \omega_g L_q i_{sq} \\ u_{sq} = -R_s i_{sq} - \dfrac{L_d}{\omega_{eb}} \dfrac{\mathrm{d}i_{sq}}{\mathrm{d}t} - \omega_g L_d i_{sd} + \omega_g \psi_f \end{cases} \tag{1}$$

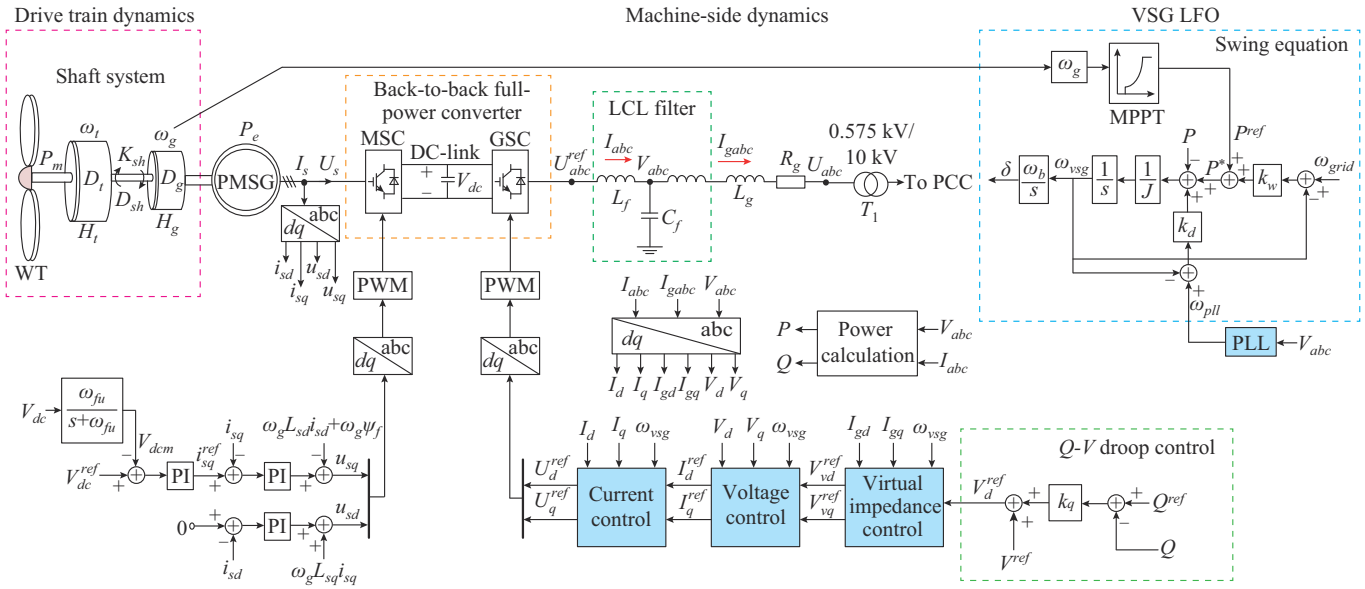

Fig. 1. Typical topological structure of grid-connected VSG-controlled PMSG-based wind generation system.

where u_{sd} and u_{sq} are the d- and q-axis stator terminal voltages, respectively; i_{sd} and i_{sq} are the d- and q-axis stator currents, respectively; R_s is the resistance of PMSG stator; ω_{eb} is the base value of stator angular frequency; ω_g is the angular velocity of generator rotor; and L_d and L_q are the d- and q-axis self-inductances of PMSG stator, respectively.

The megawatt-level PMSGs have relatively low speeds and mostly are mounted with non-salient surface ($L_d=L_q$). Therefore, the electromagnetic torque of PMSG T_e can be expressed as:

$$T_e=\psi_f i_{sq} \tag{2}$$

B. Shaft System Model

The double-mass model [23] and single-mass model [16] can be represented as (3) and (4), respectively.

$$\begin{cases} 2H_t\dfrac{\mathrm{d}\omega_t}{\mathrm{d}t}=T_m-T_{sh} \\ 2H_g\dfrac{\mathrm{d}\omega_g}{\mathrm{d}t}=T_{sh}-T_e \\ \dfrac{\mathrm{d}\theta_{sh}}{\mathrm{d}t}=\omega_{eb}(\omega_t-\omega_g) \\ T_{sh}=K_{sh}\theta_{sh}+D_{sh}(\omega_t-\omega_g) \end{cases} \tag{3}$$

$$2(H_t+H_g)\frac{\mathrm{d}\omega_g}{\mathrm{d}t}=T_m-T_e \tag{4}$$

where H_t and H_g are the inertial time constants of WT and PMSG mass blocks, respectively; ω_t is the WT speed of generator rotor; θ_{sh} is the torsion angle of WT relative to generator rotor; K_{sh} is the stiffness coefficient of shaft system; D_{sh} is the damping coefficient of shaft system; and T_m and T_{sh} are the mechanical torque and shaft system torque, respectively.

C. Model of MSC Control Section

The MSC regulates the DC-link voltage, expressed as:

$$\begin{cases} V_{dcm}=\dfrac{\omega_{fu}}{\omega_{fu}+s}V_{dc} \\ i_{sq}^{ref}=\left(K_{p1}+\dfrac{K_{i1}}{s}\right)(V_{dc}^{ref}-V_{dcm}) \\ u_{sq}=-\left(K_{p2}+\dfrac{K_{i2}}{s}\right)(i_{sq}^{ref}-i_{sq})-\omega_g L_{sd}i_{sd}-R_s i_{sd}+\omega_g\psi_f \\ u_{sd}=-\left(K_{p2}+\dfrac{K_{i2}}{s}\right)(i_{sd}^{ref}-i_{sd})+\omega_g L_{sq}i_{sq}-R_s i_{sq} \end{cases} \tag{5}$$

where V_{dc} is the DC-link voltage; V_{dcm} is the output of V_{dc} after passing through the low-pass filter (LPF); ω_{fu} is the bandwidth of MSC LPF; K_{p1} and K_{i1} are the proportional and integral coefficients of voltage outer loop in MSC, respectively; K_{p2} and K_{i2} are the proportional and integral coefficients of current inner loop in MSC, respectively; and the superscript *ref* represents the reference values.

D. LCL Filter and Grid-connected Line Model

The VSG-controlled PMSG-based wind generation system is connected to the grid through an LCL filter and grid-connected line model, which can be formulated in the dq frame of GSC as:

$$\boldsymbol{U}^{ref}=\boldsymbol{V}+\boldsymbol{Z}_{Lf}(s)\boldsymbol{I} \tag{6}$$

where $\boldsymbol{U}^{ref}=[U_d^{ref}\ \ U_q^{ref}]^{\mathrm{T}}$ is the vector of modulation voltage references for GSC; $\boldsymbol{V}=[V_d\ \ V_q]^{\mathrm{T}}$ is the vector of capacitor voltages; $\boldsymbol{I}=[I_d\ \ I_q]^{\mathrm{T}}$ is the vector of GSC currents; and $\boldsymbol{Z}_{Lf}(s)=\begin{bmatrix} L_f s/\omega_b & -\omega_{grid}L_f \\ \omega_{grid}L_f & L_f s/\omega_b \end{bmatrix}$, L_f is the converter-side inductance of LCL filter, ω_b is the base value of grid angular velocity, and ω_{grid} is the reference frequency of power grid.

$$\boldsymbol{I}=\boldsymbol{I}_g+\boldsymbol{Z}_{Cf}(s)\boldsymbol{V} \tag{7}$$

where $\boldsymbol{I}_g=[I_{gd}\ \ I_{gq}]^{\mathrm{T}}$ is the vector of grid-side currents; and $\boldsymbol{Z}_{Cf}(s)=\begin{bmatrix} C_f s/\omega_b & -\omega_{grid}C_f \\ \omega_{grid}C_f & C_f s/\omega_b \end{bmatrix}$, and C_f is the capacitance of LCL filter.

$$\boldsymbol{V}=\boldsymbol{Z}_G(s)\boldsymbol{I}_g+\boldsymbol{U} \tag{8}$$

where $\boldsymbol{U}=[U_d \quad U_q]^{\mathrm{T}}$ is the vector of grid voltages, $U_d=U\cos\delta$, $U_q=-U\sin\delta$, δ is the virtual phase angle of *dq* frame of GSC, and U is the magnitude of the grid voltage; and $\boldsymbol{Z}_G(s)=\begin{bmatrix} L_g s/\omega_b+R_g & -\omega_{grid}L_g \\ \omega_{grid}L_g & L_g s/\omega_b+R_g \end{bmatrix}$, and R_g and L_g are the grid-side resistance and inductance, respectively.

E. Model of GSC Control Section

As shown in Fig. 1, the GSC control section includes six parts: swing equation, *Q-V* droop control, virtual impedance control, voltage control, current control, and PLL.

1) Swing Equation

VSG realizes the frequency self-synchronization based on the swing equation, which represents the characteristics of the inertia and damping of SGs and can be expressed as:

$$\begin{cases} Js\omega_{vsg}=P^{ref}-P-k_d(\omega_{vsg}-\omega_{pll})-k_w(\omega_{vsg}-\omega_{grid}) \\ s\delta=\omega_b(\omega_{vsg}-\omega_{grid}) \end{cases} \tag{9}$$

where J is the virtual inertia time constant; k_d and k_w are the damping and droop coefficients of VSG, respectively; P^{ref} is the active power reference of GSC; P is the active power output of GSC; ω_{vsg} is the virtual angular frequency; and ω_{pll} is the grid frequency detected by PLL.

P^{ref} can be expressed as:

$$P^{ref}=\begin{cases} k_{opt}\omega_g^3 & v_{in}<v<v_r \\ 1 & v_r<v<v_{out} \end{cases} \tag{10}$$

where k_{opt} is the MPPT curve coefficient; v is the actual wind speed; v_r is the rated wind speed; and v_{in} and v_{out} are the cut-in and cut-out wind speeds, respectively.

2) Q-V Droop Control

The *Q-V* droop control is used for supporting the grid voltage and generating the voltage magnitude reference V_d^{ref}:

$$V_d^{ref}=V^{ref}+k_q(Q^{ref}-Q) \tag{11}$$

where V^{ref} is the external voltage magnitude reference; Q^{ref} is the reactive power reference of GSC; Q is the reactive power output of GSC; and k_q is the *Q-V* droop coefficient.

3) Virtual Impedance Control

The virtual impedance control is described as [13]:

$$\boldsymbol{V}_v^{ref}=\boldsymbol{V}_d^{ref}-\boldsymbol{Z}_v(s)\boldsymbol{I}_g \tag{12}$$

where $\boldsymbol{V}_v^{ref}=[V_{vd}^{ref} \quad V_{vq}^{ref}]^{\mathrm{T}}$ is the vector of voltage references from the virtual impedance control section; $\boldsymbol{V}_d^{ref}=[V_d^{ref} \quad 0]^{\mathrm{T}}$; and $\boldsymbol{Z}_v(s)=\begin{bmatrix} R_v & -\omega_{grid}L_v \\ \omega_{grid}L_v & R_v \end{bmatrix}$, and R_v and L_v are the virtual resistance and inductance, respectively.

4) Voltage Control

The current references for the current control are produced from the voltage control, whose dynamic equation in the *dq* frame is expressed as:

$$\boldsymbol{I}^{ref}=PI_{VCL}(s)\cdot(\boldsymbol{V}_v^{ref}-\boldsymbol{V})+\begin{bmatrix} 0 & -\omega_{gird}C_f \\ \omega_{gird}C_f & 0 \end{bmatrix}\boldsymbol{V}+k_{fi}\boldsymbol{I}_g \tag{13}$$

where $\boldsymbol{I}^{ref}=[I_d^{ref} \quad I_q^{ref}]^{\mathrm{T}}$ is the vector of current references produced from the voltage control; $PI_{VCL}(s)=K_{vp}+K_{vi}/s$ is the PI controller of voltage control; and k_{fi} is the current feedforward coefficient.

5) Current Control

The modulation voltage references of the GSC are produced from the current control loop, whose dynamic equation in the *dq* frame of current control is expressed as:

$$\boldsymbol{U}^{ref}=PI_{CCL}(s)\cdot(\boldsymbol{I}^{ref}-\boldsymbol{I})+\begin{bmatrix} 0 & -\omega_{gird}L_f \\ \omega_{gird}L & 0 \end{bmatrix}\boldsymbol{I}+K_{Vf}(s)\boldsymbol{V} \tag{14}$$

where $PI_{CCL}(s)=K_{ip}+K_{ii}/s$ is the PI controller of current control; and $K_{Vf}(s)=k_{Vf}/(s+\omega_{Vf})$ is the LPF gain, ω_{Vf} is the bandwidth, and k_{Vf} is the gain coefficient.

6) PLL

The structure of PLL can be expressed as:

$$\begin{cases} V_{qpll}=\mathrm{Im}((V_d+\mathrm{j}V_q)\mathrm{e}^{\mathrm{j}(\delta-\theta_{pll})}) \\ \omega_{pll}=PI_{pll}(s)\cdot V_{qpll}+\omega_{grid} \\ \theta_{pll}=\omega_b\omega_{pll}/s \end{cases} \tag{15}$$

where $PI_{pll}(s)=K_{ppll}+K_{ipll}/s$ is the PI controller of PLL; V_{qpll} is the *q*-axis component of $\boldsymbol{V}$ in the *dq* frame of PLL; and θ_{pll} is the phase of $\boldsymbol{V}$ in the *dq* frame of PLL.

F. Model of DC-link

The voltage dynamic of the back-to-back full-power converter is modeled by:

$$C_{dc}V_{dc}\frac{\mathrm{d}V_{dc}}{\mathrm{d}t}=P_e-P_g \tag{16}$$

$$\begin{cases} P_e=u_{sd}i_{sd}+u_{sq}i_{sq} \\ P_g=U_d^{ref}I_d+U_q^{ref}I_q \end{cases} \tag{17}$$

where P_g is the active power delivered to the grid; and C_{dc} is the DC-link capacitance.

III. Stability Analysis and Damping Enhancement Strategy

Based on the mathematical model provided in Section II, this section aims to achieve the following objectives.

1) Derive each damping component of the swing equation based on the damping torque analysis method and analyze the mechanism and regularity of machine-side dynamics of PMSG on LFOs, and compare different shaft system models.

2) Utilize the open-loop resonance analysis method to investigate the resonance mechanism between torsional oscillation and LFOs, and predict their root trajectory.

3) Propose a damping enhancement strategy to mitigate and eliminate the negative damping effect of machine-side dynamics and resonance effect.

A. Derivation of Damping Torque of VSG

According to (9), it is observed that the components affecting LFOs include P_{ref}, P, ω_{pll}, and ω_{vsg}. Based on the damping torque analysis method, we need to derive the transfer functions between these components and δ.

1) Transfer Function Between ΔP and $\Delta\delta$

Combining (6)-(8) and (12)-(14), we can obtain:

$$\boldsymbol{I}_g=\boldsymbol{Y}_V^{ref}(s)\boldsymbol{V}^{ref}+\boldsymbol{Y}_{Udq}(s)\boldsymbol{U} \tag{18}$$

where $\boldsymbol{Y}_V^{ref}(s)$ and $\boldsymbol{Y}_{Udq}(s)$ are the transfer functions of the equivalent admittance.

Linearizing (6), (7), and (18), we can obtain:

$$\Delta \boldsymbol{V} = \boldsymbol{G}_{V1}(s)\Delta\delta + \boldsymbol{G}_{V2}(s)\Delta \boldsymbol{V}^{ref} \tag{19}$$

$$\Delta \boldsymbol{I} = \boldsymbol{G}_{I1}(s)\Delta\delta + \boldsymbol{G}_{I2}(s)\Delta \boldsymbol{V}^{ref} \tag{20}$$

where $\boldsymbol{G}_{V1}(s)=[G_{V1}^{1}(s) \quad G_{V1}^{2}(s)]^{\mathrm{T}}=-(\boldsymbol{Z}_{G}(s)\boldsymbol{Y}_{Udq}(s)+\boldsymbol{E})\boldsymbol{U}_{0}$, $\boldsymbol{E}=\begin{bmatrix}1 & 0\\ 0 & 1\end{bmatrix}$, and $\boldsymbol{U}_0$ is the steady-state value of $\boldsymbol{U}$; $\boldsymbol{G}_{I1}(s)=[G_{I1}^{1}(s) \quad G_{I1}^{2}(s)]^{\mathrm{T}}=-(\boldsymbol{Z}_{Cf}(s)\boldsymbol{Z}_{G}(s)\boldsymbol{Y}_{Udq}(s)+\boldsymbol{Y}_{Udq}(s)+\boldsymbol{Z}_{Cf}(s))\boldsymbol{U}_{0}$; $\boldsymbol{G}_{V2}(s)=\begin{bmatrix}G_{V2}^{1}(s) & G_{V2}^{2}(s)\\ G_{V2}^{3}(s) & G_{V2}^{4}(s)\end{bmatrix}=\boldsymbol{Z}_{G}(s)\boldsymbol{Y}_{V}^{ref}(s)$; and $\boldsymbol{G}_{I2}(s)=\begin{bmatrix}G_{I2}^{1}(s) & G_{I2}^{2}(s)\\ G_{I2}^{3}(s) & G_{I2}^{4}(s)\end{bmatrix}=\boldsymbol{Z}_{Cf}(s)\boldsymbol{Z}_{G}(s)+\boldsymbol{E}$.

The active power and reactive power of GSC can be calculated as:

$$\begin{cases} P = V_d I_d + V_q I_q \\ Q = V_q I_d - V_d I_q \end{cases} \tag{21}$$

Formula (21) is linearized as:

$$\begin{bmatrix}\Delta P\\ \Delta Q\end{bmatrix}=\begin{bmatrix}V_{d0} & I_{d0}\\ V_{q0} & -I_{q0}\end{bmatrix}\begin{bmatrix}\Delta I_d\\ \Delta V_d\end{bmatrix}+\begin{bmatrix}V_{q0} & I_{q0}\\ -V_{d0} & I_{d0}\end{bmatrix}\begin{bmatrix}\Delta I_q\\ \Delta V_q\end{bmatrix} \tag{22}$$

where the subscript 0 represents the steady-state value.

Substituting (19) and (20) into (22) yields:

$$\begin{cases}\begin{bmatrix}\Delta P\\ \Delta Q\end{bmatrix}=\boldsymbol{S}(s)\begin{bmatrix}\Delta\delta\\ \Delta V_d^{ref}\end{bmatrix}\\ \boldsymbol{S}(s)=\begin{bmatrix}S_{11}(s) & S_{12}(s)\\ S_{21}(s) & S_{22}(s)\end{bmatrix}=\begin{bmatrix}V_{d0} & I_{d0}\\ V_{q0} & -I_{q0}\end{bmatrix}\begin{bmatrix}G_{I1}^{1}(s) & G_{I2}^{1}(s)\\ G_{V1}^{1}(s) & G_{V2}^{1}(s)\end{bmatrix}+\\ \qquad\begin{bmatrix}V_{q0} & I_{q0}\\ -V_{d0} & I_{d0}\end{bmatrix}\begin{bmatrix}G_{I1}^{2}(s) & G_{I2}^{3}(s)\\ G_{V1}^{2}(s) & G_{V2}^{3}(s)\end{bmatrix}\end{cases} \tag{23}$$

Linearizing (11), we can obtain:

$$\Delta V_d^{ref} = -k_q \Delta Q \tag{24}$$

Combining (23) with (24), the transfer function between ΔP and $\Delta\delta$, i.e., $G_P(s)$, is obtained to describe the influence of a perturbation of $\Delta\delta$ on the active power of the swing equation:

$$\Delta P = \left(S_{11}(s) - \frac{k_q S_{21}(s) S_{12}(s)}{1 + k_q S_{22}(s)}\right)\Delta\delta = G_P(s)\Delta\delta \tag{25}$$

The detailed derivation of (25) is shown in Supplementary Material B.

2) Transfer Function Between $\Delta\omega_{pll}$ and $\Delta\delta$

In this part, we derive the transfer function between $\Delta\omega_{pll}$ and $\Delta\delta$, i.e., $G_{pll}(s)$, to reflect the impact of PLL on LFOs.

Linearizing (15), we can obtain:

$$\begin{cases}\Delta V_{qpll} = \Delta V_q \cos(\delta_0 - \theta_{pll0}) - V_{q0}\sin(\delta_0 - \theta_{pll0})(\Delta\delta - \Delta\theta_{pll}) + \\ \qquad \Delta V_d \sin(\delta_0 - \theta_{pll0}) + V_{d0}\cos(\delta_0 - \theta_{pll0})(\Delta\delta - \Delta\theta_{pll})\\ \Delta\omega_{pll} = PI_{pll}(s)\cdot\Delta V_{qpll}\\ \Delta\theta_{pll} = \omega_b \Delta\omega_{pll}/s\end{cases} \tag{26}$$

Combining (26) with (19), (20), (22), and (23), we can obtain:

$$\begin{cases}\Delta\omega_{pll} = \left[\dfrac{P_1(s)}{P_3(s)} - \dfrac{P_2(s)k_q S_{21}(s)}{P_3(s)(1+k_q S_{22}(s))}\right]\Delta\delta = G_{wpll}(s)\Delta\delta\\ P_1(s) = G_{V1}^{2}(s)\cos(\delta_0 - \theta_{pll0}) + G_{V1}^{1}(s)\sin(\delta_0 - \theta_{pll0}) + m\\ P_2(s) = G_{V2}^{3}(s)\cos(\delta_0 - \theta_{pll0}) + G_{V2}^{1}(s)\sin(\delta_0 - \theta_{pll0})\\ P_3(s) = m\omega_b/s + 1/(PI_{pll}(s))\\ m = V_{d0}\cos(\delta_0 - \theta_{pll0}) - V_{q0}\sin(\delta_0 - \theta_{pll0})\end{cases} \tag{27}$$

The detailed derivation of (27) is shown in Supplementary Material C.

3) Transfer Function Between $\Delta\omega_g$ and $\Delta\delta$

Based on (9) and (10), it is apparent that the VSG-controlled PMSG-based wind generation system predominantly operates in the MPPT mode, where the active power reference $P^{ref}=k_{opt}\omega_g^3$. Consequently, the machine-side dynamics of PMSG invariably influence LFOs on the grid side.

The transfer function between $\Delta\omega_g$ and $\Delta\delta$ captures the influence of machine-side dynamics of PMSG on LFOs.

By linearizing (1), we derive the transfer function between $\Delta\omega_g$ and $\Delta\omega_t$, i.e., $G_{wt}(s)$, as:

$$\Delta\omega_t = \frac{D_{sh}s + K_{sh}\omega_{eb}}{2H_t s^2 + D_{sh}s + K_{sh}\omega_{eb}}\Delta\omega_g = G_{wt}(s)\Delta\omega_g \tag{28}$$

Linearizing (2)-(4), the transfer function between $\Delta\omega_g$ and Δi_{sq} is derived as:

$$\Delta i_{sq} = \begin{cases} -\dfrac{2s}{\psi_f}\left[\dfrac{2H_t H_g s^2 + (H_t + H_g)D_{sh}s + (H_t + H_g)K_{sh}\omega_{eb}}{2H_t s^2 + D_{sh}s + K_{sh}\omega_{eb}}\right]\Delta\omega_g = \\ \qquad G_{wg,\,\mathrm{double}}(s)\Delta\omega_g \quad \text{under doulbe-mass model} \\ -\left[\dfrac{2(H_t + H_g)\omega_{g0}s + \psi_f i_{sq0}}{\psi_f \omega_{g0}}\right]\Delta\omega_g = G_{wg,\,\mathrm{single}}(s)\Delta\omega_g \\ \qquad \text{under single-mass model}\end{cases} \tag{29}$$

where $G_{wg,\,\mathrm{double}}(s)$ and $G_{wg,\,\mathrm{single}}(s)$ are the transfer functions between $\Delta\omega_g$ and Δi_{sq} under the double-mass and single-mass models, respectively.

By linearizing (1) and (5), the transfer function between Δi_{sq} and ΔV_{dc}, i.e., $G_{Vdc}(s)$, is obtained as:

$$\Delta V_{dc} = -\frac{(\omega_{fu} + s)(L_{sq}s + \omega_{eb}\cdot PI_2(s))}{s\omega_{eb}\cdot PI_1(s)\cdot PI_2(s)}\Delta i_{sq} = G_{Vdc}(s)\Delta i_{sq} \tag{30}$$

where $PI_1(s)=K_{p1}+K_{i1}/s$; and $PI_2(s)=K_{p2}+K_{i2}/s$.

Linearizing (16), we can yield:

$$C_{dc}V_{dc0}\Delta V_{dc}s/\omega_b = u_{sq0}\Delta i_{sq} + i_{sq0}\Delta u_{sq} - \Delta P_g \tag{31}$$

Combining (29)-(31), we can obtain:

$$\Delta P \approx \Delta P_g = G_{Pg}(s)\Delta\omega_g \tag{32}$$

where $G_{Pg}(s)$ is the transfer function between ΔP and ω_g.

The detailed derivation of (32) is shown in Supplementary Material D.

Combining (25) and (32), we can obtain:

$$\Delta\omega_g = \frac{G_P(s)}{G_{Pg}(s)}\Delta\delta = G_{wg}(s)\Delta\delta \tag{33}$$

Linearizing (8) and combining the transfer functions in (25), (27), and (33), the linearized swing equation can be represented by the closed-loop block diagram in Fig. 2

based on the damping torque analysis method, which reflects the damping dynamic of LFOs considering machine-side dynamics. As depicted in Fig. 2, four feedback loops are identified: machine-side, active power, damping, and PLL feedback loops. According to the damping torque analysis method, four equivalent torques ΔT_{wg}, ΔT_P, ΔT_{pll}, and ΔT_d influence LFOs, where ΔT_{wg} represents the impact of machine-side dynamics; ΔT_P represents the impact of active power; ΔT_{pll} represents the impact of PLL; and ΔT_d represents the impact of k_d. The transfer functions between the four equivalent torques and $\Delta\delta$ are $f_{wg}(s)$, $f_P(s)$, $f_{pll}(s)$ and $f_d(s)$, respectively.

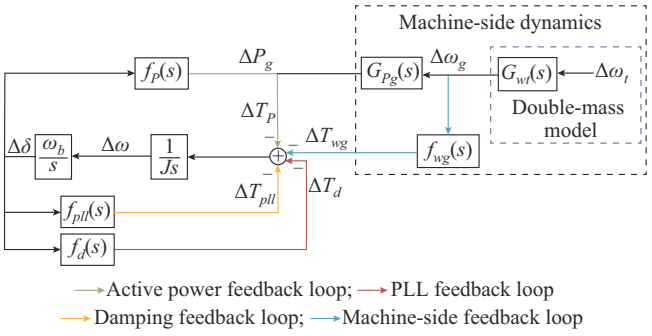

Fig. 2. Closed-loop transfer block diagram and equivalent torque of VSG-controlled PMSG-based wind generation systems.

The linearized swing equation can be formulated as:

$$J\Delta\delta = -\Delta T_{wg} - \Delta T_P - \Delta T_d - \Delta T_{pll} \tag{34}$$

where $\Delta T_{wg} = -3k_{opt}\omega_{g0}^2\Delta\omega_g = f_{wg}(s)\Delta\delta$; $\Delta T_P = \Delta P = f_P(s)\Delta\delta$; $\Delta T_d = -k_d\Delta\omega_{vsg} = (-k_d s/\omega_b)\Delta\delta = f_d(s)\Delta\delta$; and $\Delta T_{pll} = -k_d\Delta\omega_{pll} = f_{pll}(s)\Delta\delta$.

According to the damping torque analysis method, the torque ΔT_Σ can be decomposed into two components: ① damping torque $\Delta T_{\Sigma,D}$, which determines the damping of LFOs, and ② synchronizing torque $\Delta T_{\Sigma,S}$, which affects the synchronizing ability of rotor and the frequency of LFOs [24]. The damping torque aligns positively with virtual angular frequency $\Delta\omega_{vsg}$ and the synchronizing torque aligns positively with the angle $\Delta\delta$. Furthermore, the system is stable if ΔT_Σ is decomposed into positive damping and synchronizing torques across all frequencies. The negative damping torque leads to LFOs in active power and rotor speed. Conversely, the negative synchronizing torque results in loss of phase synchronization with the power grid, indicated by the rotor angle continuously deviating from the grid voltage angle instead of oscillations [7].

Because the synchronizing torque does not affect the system damping, only the damping torque determines the damping magnitude. To this end, it is necessary to ensure that the synchronizing torque remains positive when studying the effect of damping torque on stability. The composite damping torque can be calculated using:

$$\begin{aligned}\Delta T_{\Sigma,D} = \Delta T_{wg,D} + \Delta T_{P,D} + \Delta T_{d,D} + \Delta T_{pll,D} = \left|\Delta T_{wg}\right|\sin\delta_{wg} + \\ \left|\Delta T_P\right|\sin\delta_P + \left|\Delta T_d\right|\sin\delta_d + \left|\Delta T_{pll}\right|\sin\delta_{pll}\end{aligned} \tag{35}$$

where the subscript D represents the damping torque components; and δ_{wg}, δ_P, δ_d, and δ_{pll} are the angles between ΔT_{wg}, ΔT_P, ΔT_d, ΔT_{pll} and the positive direction of $\Delta\delta$, respectively.

The Bode diagram of each transfer function are depicted in Fig. 3.

Since the frequency of LFOs typically ranges from 0.1 to 2 Hz, our analysis focuses on examining the damping characteristics within this frequency range. Within 0.1-2 Hz, the phase characteristics of the transfer functions are as follows. $f_P(s)$ spans a phase range between −7° - 0°, mainly contributing to positive synchronizing torque with a minor negative damping component. The phase of $f_{pll}(s)$ is approximately −90°, primarily indicating negative damping. The phase of $f_d(s)$ is approximately 90°, indicating positive damping. When using the single-mass model, the phase of $f_{wg}(s)$ is approximately 90°, primarily indicating negative damping. However, when using the double-mass model, although the phase of $f_{wg}(s)$ is also around 90°, two resonance points exist at frequencies of $f_1 = 0.94$ Hz and $f_2 = 2.54$ Hz. Within 0.94-2.54 Hz, the phase of $f_{wg}(s)$ shifts to −90°. This phenomenon can be explained as follows. According to (33), the magnitude and phase of $f_{wg}(s)$ depend on $G_P(s)$ and $G_{Pg}(s)$, where $G_P(s) = f_P(s)$. $G_{Pg}(s)$ is primarily influenced by the shaft system parameters, PMSG parameters, control parameters, and DC-link voltage loop. Additionally, based on Fig. 4, there is a clear distinction between $\Delta T_{\Sigma,D,d}$, $\Delta T_{\Sigma,D,s}$, and $\Delta T_{\Sigma,D,s}^{VSG}$, where the subscripts d and s represent that the double-mass model and single-mass model are considered, and the superscript VSG represents the machine-side dynamics are not considered. The double-mass model is crucial for accurately evaluating the LFOs due to the presence of resonance points. As shown in Fig. 5, when considering the double-mass model and the frequency of LFOs being outside the range of $[f_1, f_2]$, $\Delta T_{wg,D}$ is less than 0, providing negative damping for LFOs. Conversely, when the frequency of LFOs falls within the range of $[f_1, f_2]$, $\Delta T_{wg,D}$ is greater than 0, offering positive damping for LFOs.

The conclusions drawn from Figs. 3-5 are as follows.

1) When the double-mass model is adopted for the shaft system and the frequency of LFOs is outside the range of $[f_1, f_2]$, the phase of $f_{wg}(s)$ aligns approximately at −90°, consistent with the single-mass model. As the frequency of LFOs approaches f_1, the double-mass model exhibits a smaller magnitude of $f_{wg}(s)$ than the single-mass model due to resonance points, resulting in weaker negative damping effects. Conversely, when approaching f_1 from the right side, the double-mass model exhibits a greater magnitude of $f_{wg}(s)$, leading to stronger negative damping effects.

2) When the frequency of LFOs falls within the range of $[f_1, f_2]$, the phase of $f_{wg}(s)$ approaches approximately 90°, indicating that the machine side provides positive damping to LFOs.

Therefore, by examining Fig. 3(a) and (c) with the expression of $G_{Pg}(s)$, it finds that two resonance points in $f_{wg}(s)$ are derived from (29). The frequencies corresponding to these resonance points can be determined as:

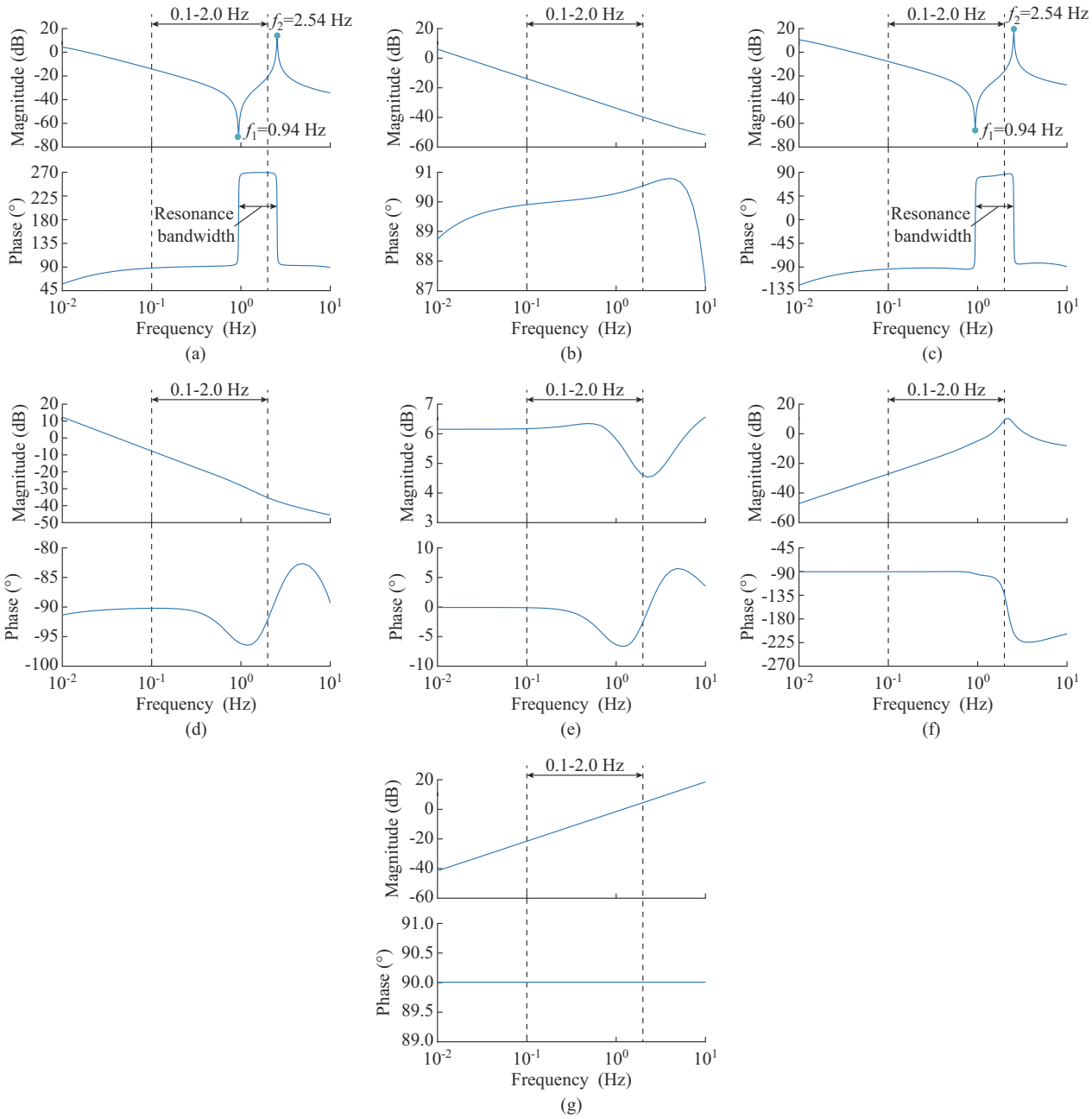

Fig. 3. Bode diagram of each transfer function. (a) $1/G_{Pg}(s)$ of double-mass model. (b) $1/G_{Pg}(s)$ of single-mass model. (c) $f_{wg}(s)$ of double-mass model. (d) $f_{wg}(s)$ of single-mass model. (e) $f_P(s)$. (f) $f_{pll}(s)$. (g) $f_d(s)$.

$$\begin{cases} f_1 = \dfrac{1}{2\pi}\sqrt{\dfrac{\omega_{eb}K_{sh}}{2H_t}} \\ f_2 = \dfrac{1}{2\pi}\sqrt{\omega_{eb}K_{sh}\left(\dfrac{1}{2H_g}+\dfrac{1}{2H_t}\right)} \end{cases} \tag{36}$$

Using the values in Supplementary Material A Table SAI and substituting them into (36), we can obtain $f_1 = 0.94$ Hz and $f_2 = 1.54$ Hz, which are consistent with the resonance frequencies of $f_{wg}(s)$. It can be observed that: ① f_2 is always greater than f_1. ② f_2 represents the torsional oscillation frequency, determined by K_{sh}, H_g, and H_t. ③ f_1 is determined by K_{sh} and H_t. ④ The bandwidth of f_1 and f_2 is determined by H_g and H_t.

B. Influence Mechanisms of Parameters on LFOs

After the derivation of the damping torque of VSG, this subsection focuses on investigating the influence mechanisms of parameters on LFOs. As discussed in [7], the phase of $f_P(s)$ remains approximately 90° within the frequency range of LFOs despite variations in grid-side parameters such as k_d, L_f, L_g, and L_v. Modifying L_g alters the magnitude of $f_P(s)$, consequently impacting $f_{wg}(s)$. Besides, the influence of machine-side dynamics on LFOs primarily hinges on machine-side parameters, encompassing H_g, H_t, K_{sh}, D_{sh}, and C_{dc}. The Bode diagrams of $f_{wg}(s)$ and damping torque components $\Delta T_{\Sigma,D}$, ΔT_{wg}, ΔT_P, ΔT_{pll}, and ΔT_d with different values of L_g, H_g, H_t, H=H_g+H_t, K_{sh}, D_{sh}, and C_{dc} are depicted in Supplementary Material E Figs. SE1 and SE2.

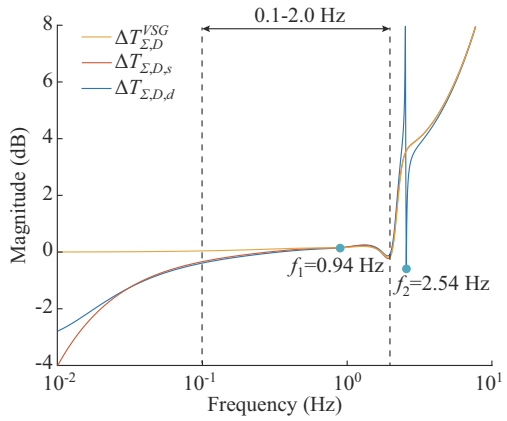

Fig. 4. Damping torques $\Delta T_{\Sigma,D,d}$, $\Delta T_{\Sigma,D,s}$, and $\Delta T_{\Sigma,D,s}^{VSG}$

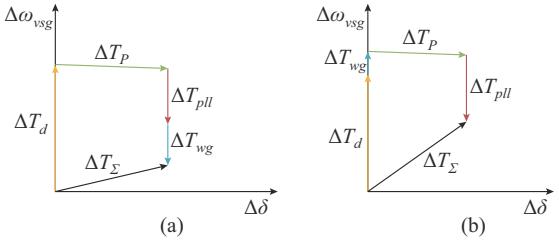

Fig. 5. Equivalent torque in VSG-controlled *dq* frame. (a) Frequency of LFOs is outside $[f_1, f_2]$. (b) Frequency of LFOs is within $[f_1, f_2]$ with double-mass model.

In Figs. SE1(a)-(d) and SE2(a)-(d), with an increase in L_g, the magnitude of $f_{wg}(s)$ decreases, ΔT_{wg} increases, and ΔT_{pll} decreases. When the frequency of LFO is outside $[f_1, f_2]$, $\Delta T_{\Sigma,D}$ increases, while $\Delta T_{\Sigma,D}$ decreases. Additionally, with an increase in H_g, f_2 decreases, leading to a narrower resonance bandwidth. The magnitude of $f_{wg}(s)$ within $(0, f_1)$ decreases, but increases within $[f_1, f_2]$, resulting in an increase in $\Delta T_{\Sigma,D}$. Similarly, an increase in H_t causes f_1 and f_2 to decrease simultaneously, widening the resonance bandwidth. The magnitude of $f_{wg}(s)$ within $(0, f_1)$ decreases, while $\Delta T_{\Sigma,D}$ increases. Furthermore, an increase in H results in a simultaneous decrease in f_1 and f_2, widening the resonance bandwidth. The magnitude of $f_{wg}(s)$ within $(0, f_1)$ decreases, leading to an increase in $\Delta T_{\Sigma,D}$.

In Figs. SE1(e)-(g) and SE2(e)-(g), an increase in K_{sh} results in simultaneous increases in f_1 and f_2, widening the resonance bandwidth. The magnitude of $f_{wg}(s)$ within $(0, f_1)$ increases, while $\Delta T_{\Sigma,D}$ decreases. Conversely, f_1, f_2, and the resonance bandwidth remain unchanged with an increase in D_{sh}. The magnitude of $f_{wg}(s)$ within the resonance bandwidth also remains unchanged, but the phase decreases, weakening the positive damping effect and reducing the resonance peak. Additionally, an increase in C_{dc} does not affect f_1, f_2, or the resonance bandwidth. The magnitude within the resonance bandwidth remains unchanged, and the phase remains constant. However, the resonance peak frequency of the DC-link voltage loop decreases, approaching f_2. It is observed that when H_t and H_g are difficult to change, increasing K_{sh}, J, and L_g can place the frequency of LFOs within the resonance bandwidth, approaching f_2 to increase the magnitude and positive damping effect. However, the frequency of LFOs should not approach f_2 too closely because the resonance may occur, leading to decreased system stability. After determining the resonance frequency range and ensuring the shaft damping, a moderate decrease in D_{sh} can improve the stability in low-frequency range. C_{dc} should not be too large, as it may cause the two resonance peaks to approach each other. Supplementary Material E Table SEI shows the summary of influence laws.

C. Resonance Analysis Between Torsional Oscillation and LFOs

Define $\boldsymbol{X}_m$ as the column vector encompassing all state variables on the machine side. The state-space model for the machine-side system can be derived as:

$$\begin{cases} s\Delta\boldsymbol{X}_m = \boldsymbol{A}_m\Delta\boldsymbol{X}_m + \boldsymbol{b}_m\Delta P_g \\ \Delta\omega_g = \boldsymbol{C}_m\Delta\boldsymbol{X}_m + d_m\Delta P_g \\ \Delta\omega_g = G_m(s)\Delta P_g \end{cases} \tag{37}$$

where $\boldsymbol{A}_m$ is the open-loop state matrix of the machine-side system; $\boldsymbol{b}_m$, $\boldsymbol{C}_m$, and d_m are the input vector, output vector, and control coefficients of the machine-side system, respectively; and $G_m(s)=\boldsymbol{C}_m(s\boldsymbol{E}-\boldsymbol{A}_m)^{-1}\boldsymbol{b}_m+d_m=1/G_{Pg}(s)$.

Define $\boldsymbol{X}_g$ as the column vector comprising all state variables on the grid side. The state-space model for the grid-side subsystem can be derived as follows:

$$\begin{cases} s\Delta\boldsymbol{X}_g = \boldsymbol{A}_g\Delta\boldsymbol{X}_g + \boldsymbol{b}_g\Delta\omega_g \\ \Delta P_g = \boldsymbol{C}_g\Delta\boldsymbol{X}_g + d_g\Delta\omega_g \\ \Delta P_g = G_g(s)\Delta\omega_g \end{cases} \tag{38}$$

where $\boldsymbol{A}_g$ is the open-loop state matrix of the grid-side system; $\boldsymbol{b}_g$, $\boldsymbol{C}_g$, and d_g are the input vector, output vector, and control coefficients of the grid-side system, respectively; and $G_g(s)=\boldsymbol{C}_g(s\boldsymbol{E}-\boldsymbol{A}_g)^{-1}\boldsymbol{b}_g+d_g$.

Based on the open-loop resonance analysis method, the VSG-controlled PMSG-based wind generation system can be divided into machine-side and grid-side systems [19].

Figure 6 illustrates the derivation of (7), i.e., the closed-loop state-space model for the VSG-controlled PMSG-based wind generation system, as given in (39).

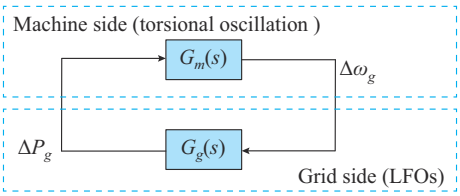

Fig. 6. Closed-loop state-space model of VSG-controlled PMSG-based wind generation system.

$$\begin{cases} s\Delta\boldsymbol{X} = \boldsymbol{A}\Delta\boldsymbol{X} \\ \Delta\boldsymbol{X} = [\Delta\boldsymbol{X}_m^{\mathrm{T}} \quad \Delta\boldsymbol{X}_g^{\mathrm{T}}]^{\mathrm{T}} \\ \boldsymbol{A} = \begin{bmatrix} \boldsymbol{A}_g + \dfrac{d_m\boldsymbol{b}_g\boldsymbol{C}_g}{1-d_md_g} & \dfrac{\boldsymbol{b}_g\boldsymbol{C}_m}{1-d_md_g} \\ \dfrac{\boldsymbol{b}_m\boldsymbol{C}_g}{1-d_md_g} & \boldsymbol{A}_m + \dfrac{d_g\boldsymbol{b}_m\boldsymbol{C}_m}{1-d_md_g} \end{bmatrix} \end{cases} \tag{39}$$

λ_m and λ_g are defined as the open-loop modes of machine-side and grid-side systems, respectively. When the distance between λ_m and λ_g is close, the strong dynamic interaction between the machine-side and grid-side systems may occur. Since λ_m is the pole of the transfer function $G_m(s)$ on the complex plane, $|G_m(\lambda_m)|$ is large. Therefore, $G_g(\lambda_g)$ will also be large when $\lambda_m \approx \lambda_g$, resulting in a strong dynamic interaction between the two systems. Based on the residue method [25], (40) can characterize the influence of dynamic interactions.

$$\begin{cases} \Delta\lambda_m = \hat{\lambda}_m - \lambda_m \\ \Delta\lambda_g = \hat{\lambda}_g - \lambda_g \end{cases} \tag{40}$$

Under the condition of open-loop resonance mode, i. e., $\lambda_m \approx \lambda_g$, the root loci corresponding to $\hat{\lambda}_m$ and $\hat{\lambda}_g$ in the closed-loop mode will be distributed on both sides of those in the open-loop mode.

$$\begin{cases} \hat{\lambda}_m = \lambda_m \pm \Delta\lambda_m = \lambda_m \pm \sqrt{R_{ms}R_{gs}} \\ \hat{\lambda}_g = \lambda_g \pm \Delta\lambda_g = \lambda_g \pm \sqrt{R_{ms}R_{gs}} \end{cases} \tag{41}$$

where R_{ms} and R_{gs} are the residues of the machine-side and grid-side systems, respectively.

If $\mathrm{Re}(\sqrt{R_{ms}R_{gs}})$ exceeds the real part of either λ_m or λ_g, it indicates the negative damping in the oscillation mode of closed-loop system and the loss of stability. $\mathrm{Re}(\sqrt{R_{ms}R_{gs}})$ serves as an estimator for the open-loop mode coupling and closed-loop mode.

An analysis of the potential resonance phenomenon between torsional oscillation and LFOs is undertaken. The inertia time constant $H = H_g + H_t$ systematically varies from 0.5 to 40 s with an increment of 0.5 s. The root loci and damping ratios of open-loop and closed-loop LFOs and torsional oscillations are obtained under both single-mass and double-mass models, as shown in Figs. 7 and 8, respectively. Note that the torsional oscillation does not exist under the single-mass model. The corresponding normalized participation factors (NPFs) of the states associated with shaft system and VSG are delineated in Fig. 9.

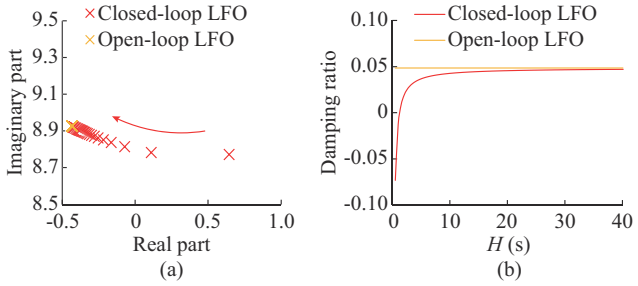

Fig. 7. Root loci and damping ratios of close-loop and open-loop LFOs under single-mass model. (a) Root loci. (b) Damping ratios.

As shown in Fig. 7, with the increase in H under the single-mass model, it can be observed that the closed-loop LFO gradually approaches the open-loop LFO. The damping ratio of closed-loop LFO increases gradually, approaching that of the open-loop LFO, while the negative damping effect of machine-side dynamics on the LFOs diminishes gradually, which is consistent with the previous theoretical analysis.

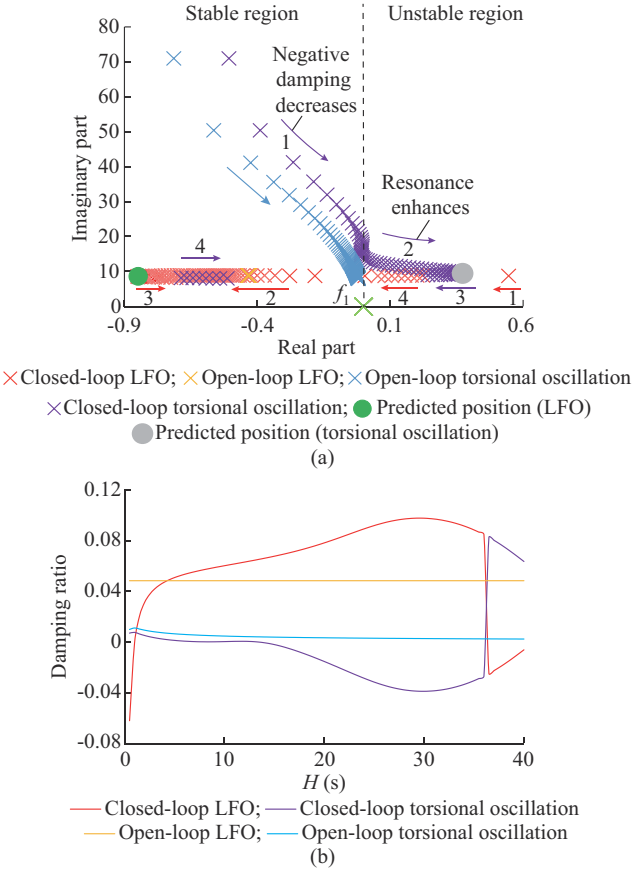

Fig. 8. Root loci and damping ratios of closed-loop and open-loop LFOs and torsional oscillations under double-mass model. (a) Root loci. (b) Damping ratios.

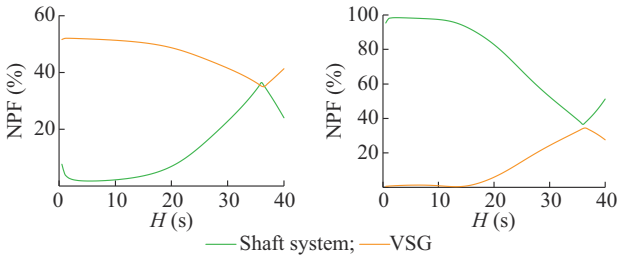

Fig. 9. NPFs of states associated with shaft system and VSG with different oscillation modes. (a) LFO. (b) Torsional oscillation.

As depicted in Figs. 8 and 9, when employing the double-mass model, with the increase in H, the closed-loop LFO gradually approaches the open-loop LFO, with the damping ratio increasing and the negative damping effect decreasing gradually.

When H increases to 6 s, the damping ratio of closed-loop LFO exceeds that of the open-loop LFO, resulting in the transition of negative damping effect to positive damping effect of the machine-side dynamics on the LFOs. Furthermore, as H continues to increase, the resonance gradually occurs between LFO and torsional oscillation. When $H = 10$ s, where λ_m and λ_g are relatively distant, the interaction be-

tween LFO and torsional oscillation is limited, with the NPFs of the states associated with the shaft system contributing only 4% to LFO. However, when $H=30$ s, where $\hat{\lambda}_m$ and $\hat{\lambda}_g$ are closer, a strong interaction occurs between them, with the NPFs of the states associated with the shaft system contributing 22.8% to LFO, while the NPFs of the states associated with the VSG contributing 41.4% to torsional oscillation. Additionally, utilizing the residue method at this point yields $\sqrt{R_m R_g}=0.303+\mathrm{j}0.0394$, indicating a close approximation between the predicted and actual positions.

D. Damping Enhancement Strategy of LFOs

When the frequency of LFOs falls outside $[f_1, f_2]$, the phase compensation method can mitigate the negative damping effect on the machine side. This method focuses on altering the phase of $f_{wg}(s)$ in the low-frequency range using the phase compensation controller $H_i(s)$, whose transfer function is expressed as:

$$H_i(s)=\left(\frac{1+sT_1}{1+sT_2}\right)^2 \tag{42}$$

where T_1 and T_2 are the lead and lag correction time constants, respectively.

The structure of GSC control section with $H_i(s)$ added is illustrated in Fig. 10(a). This addition alters the closed-loop transfer block diagram accordingly. The inclusion of $H_i(s)$ in P_{ref} of the swing equation compensates for the negative damping impact of $f_{wg}(s)$ on the frequency of LFOs by adjusting the phase to approach 0°.

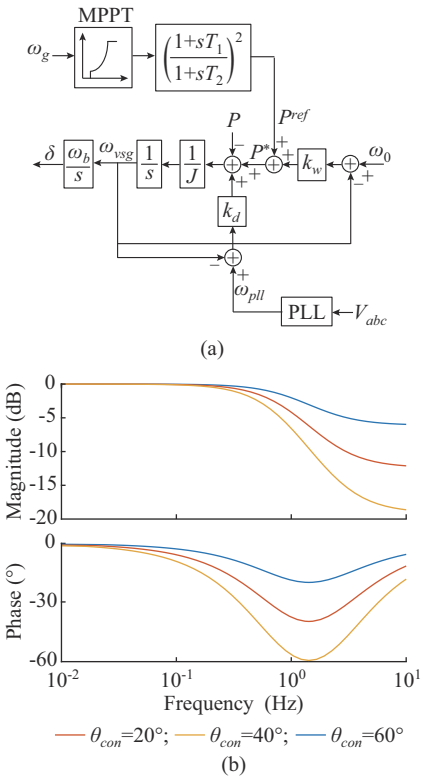

Fig. 10. Structure of GSC control section with $H_i(s)$ added and Bode diagram of $H_i(s)$ with different θ_{con}. (a) Structure of GSC control section with $H_i(s)$ added. (b) Bode diagram of $H_i(s)$ with different θ_{con}.

Figure 10(b) depicts the Bode diagram of $H_i(s)$ with various compensation angles θ_{con}. An increase in θ_{con} results in a decrease in magnitude, diminishing the system active response. Therefore, it is crucial to find a balance between θ_{con} and system active response. Figure 11 shows the closed-loop transfer block diagram of the VSG-controlled PMSG-based wind generation systems with $H_i(s)$ added. Figure 12 displays the damping torque components with different θ_{con} of $H_i(s)$. Notably, ΔT_{wg} and $\Delta T_{\Sigma,D}$ rise with θ_{con}, mitigating the negative damping effect of the machine-side dynamics and bolstering the damping of LFOs, thereby improving the system stability.

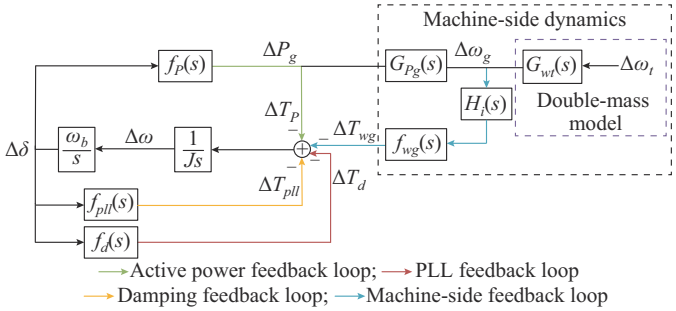

Fig. 11. Closed-loop transfer block diagram of VSG-controlled PMSG-based wind generation systems with $H_i(s)$ added.

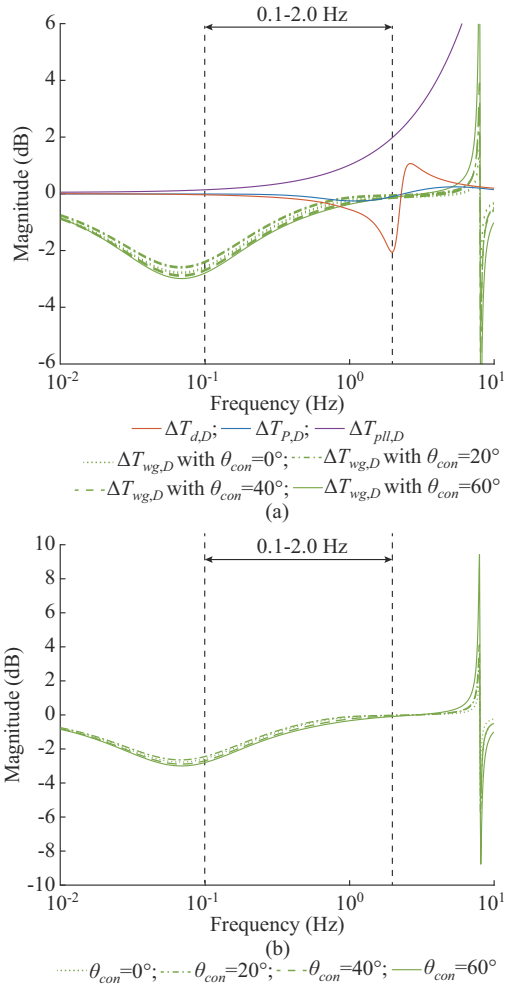

Fig. 12. Damping torque components with different θ_{con}. (a) $\Delta T_{wg,D}$, $\Delta T_{P,D}$, $\Delta T_{pll,D}$, and $\Delta T_{d,D}$.(b) $\Delta T_{\Sigma,D}$.

Based on the above analysis, a damping enhancement strategy of LFOs in VSG-controlled PMSG-based wind generation systems is proposed.

Step 1: establish the small-signal model of the system and calculate the frequencies of torsional oscillation and LFO using eigenvalue analysis. Compute f_1 and f_2 based on (36).

Step 2: plot the Bode diagrams of $f_{wg}(s)$, $f_P(s)$, $f_{pll}(s)$, and $f_d(s)$ based on (34), and predict the root locus of LFO and torsional oscillation using the residue method, obtaining $\mathrm{Re}(\sqrt{R_m R_g})$.

Step 3: check if the frequency of LFOs is within $[f_1, f_2]$. If it is within this range and $\mathrm{Re}(\sqrt{R_m R_g})$ is relatively large, adjust the values of L_g and J within a reasonable range to make the frequency of LFOs close to f_1 and $\mathrm{Re}(\sqrt{R_m R_g})$ relatively small; else, go to *Step 4*.

Step 4: add $H_i(s)$ to the VSG and calculate T_1 and T_2 based on $f_{wg}(s)$, and solve (27) and (28) to determine the time constants of the lead-lag compensator with a desired phase lag at the frequency of LFOs.

IV. Simulink Results and Discussion

This section aims to validate the prior theoretical analyses concerning damping torque and damping enhancement strategies of LFOs and to study the dynamic performance of the VSG-controlled PMSG-based wind generation system. A VSG-controlled PMSG-based wind generation system connected to the IEEE 39-bus AC grid, as depicted in Fig. 13, is implemented using the MATLAB/Simulink platform.

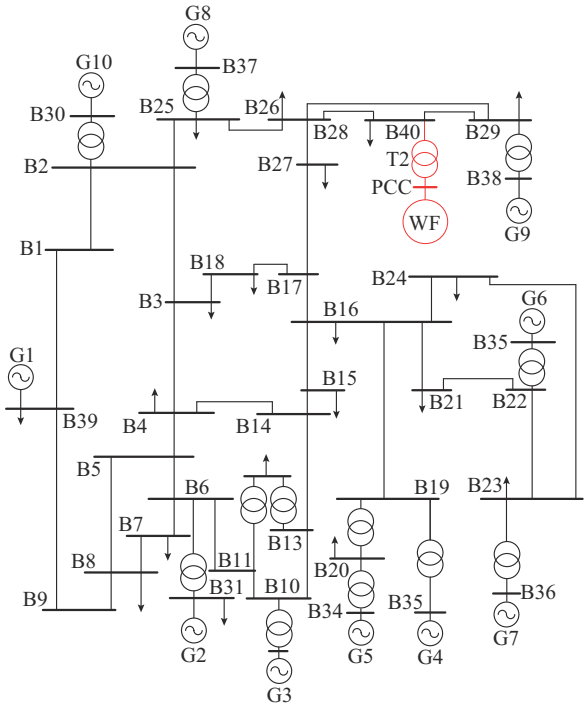

Fig. 13. A VSG-controlled PMSG-based wind generation system connected to IEEE 39-bus AC grid.

The base active power of the VSG-controlled PMSG-based wind generation system is 400 MW. The parameters for the VSG-controlled PMSG-based wind generation system and SGs are provided in Supplementary Material A Table SAI and Supplementary Material F Table SFI, respectively, with D_{sh} modified to 2 p.u.. A constant wind speed of 12.1 m/s, corresponding to the rated wind speed, is maintained throughout the simulation. At $t=120$ s of the simulation, a temporary three-phase short-circuit fault occurs at bus B40, which is cleared within 0.1 s.

A. Verification of Necessity of Double-mass Model

This subsection aims to validate the necessity of employing the double-mass model and investigate the resonant effects of torsional oscillation and LFOs. The transient response curves of the system under different values of H using the single-mass model are shown in Supplementary Material G Fig. SG1. It is observed that with the increase in H, U_{dc}, P, U, ω_{vsg}, P_{line}, and $\delta_{8\text{-}9}$ transition from divergence to convergence when employing the single-mass model, accompanied by a decrease in oscillation magnitude and an increase in damping rate, which indicates a gradual weakening of the negative damping effect of machine-side dynamics on LFOs.

The transient response curves of the system under different values of H using the double-mass model are shown in Supplementary Material G Fig. SG2. When using the double-mass model, as H increases, U_{dc}, P, U, ω_{vsg}, P_{line}, and $\delta_{8\text{-}9}$ first transition from divergence to convergence, accompanied by a decrease in oscillation magnitude and an increase in damping rate, which indicates a gradual weakening of the negative damping effect of machine-side dynamics on LFOs. As H continues to increase at 5 s, it is observed that the oscillation magnitudes of U_{dc}, P, U, ω_{vsg}, P_{line}, and $\delta_{8\text{-}9}$ increase while the damping rate decreases. When H reaches 15 s, the system becomes unstable. This phenomenon indicates an enhancement in the resonant effects of torsional oscillation and LFOs, consistent with previous theoretical analyses, thus demonstrating the necessity of employing the double-mass model.

B. Verification of Proposed Damping Enhancement Strategy

This subsection verifies the effectiveness of the proposed damping enhancement strategy in two scenarios: ① the resonance between torsional oscillation and LFOs is weak and the negative damping is strong ($H=5$ s), and ② the resonance between torsional oscillation and LFOs is strong, and the frequency of LFOs lies within $[f_1, f_2]$ ($H=15$ s). As shown in Supplementary Material H Fig. SH1, when $H=5$ s, increasing θ_{con} of $H_i(s)$ results in a reduction in the oscillation magnitude of U_{dc}, P, U, ω_{vsg}, P_{line}, and $\delta_{8\text{-}9}$, along with an increase in damping rate, demonstrating the effectiveness of $H_i(s)$ in suppressing the negative damping and the beneficial effect of increasing θ_{con}.

Using the residue method, we vary J and L_g. When $J=8$ and $L_g=0.05$ p. u., $\mathrm{Re}(\sqrt{R_m R_g})$ decreases the most from 0.256 to 0.07, indicating a weakening of the resonance. The transient responses with different values of J and L_g are depicted in Supplementary Material H Fig. SH2. It is observed that when $J=8$ and $L_g=0.05$ p.u., the oscillation magnitudes

of U_{dc}, P, U, ω_{vsg}, P_{line}, and $\delta_{8\text{-}9}$ are minimized, while the damping rate is maximized, leading to system re-stabilization. This decrease in L_g results in the torsional oscillation and LFO modes moving further apart in the complex plane, thereby reducing $\mathrm{Re}(\sqrt{R_m R_g})$, diminishing their coupling effect, and enhancing the system stability.

V. Conclusion

This paper elucidates the influence of machine-side dynamics on LFOs and compares the effects of single-mass and double-mass models on LFOs. It enables quantitative assessment of the damping effects of each torque component on LFOs and reveals the impact of different parameters on them based on the damping torque analysis method. It is found that employing double-mass models results not only in negative damping but also in positive damping within [f_1, f_2] due to the resonance points, demonstrating the necessity of the double-mass model for precise stability analysis.

Next, this paper employs the open-loop resonance analysis method to explore the resonance mechanism between torsional oscillation and LFOs. It is noted that improper parameter selection can induce the resonance due to their close root loci on the complex plane. Moreover, the residue method is used to predict the root loci accurately. Subsequently, a corresponding damping enhancement strategy is proposed to alleviate the machine-side negative damping effects and avert strong resonance between torsional oscillation and LFOs.

Finally, a time-domain simulation model for VSG-controlled PMSG-based wind generation systems connected to the IEEE 39-bus AC grid is developed in MATLAB/Simulink to validate the accuracy of the theoretical analysis and the effectiveness of the proposed damping enhancement strategy.

References

[1] Z. Zhuo, N. Zhang, X. Xie *et al*. "Key technologies and developing challenges of power system with high proportion of renewable energy," *Automation of Electric Power Systems*, vol. 45, no. 9, pp. 171-191, Aug. 2021.

[2] W. Zhang, W. Sheng, Q. Duan *et al*., "Automatic generation control with virtual synchronous renewables," *Journal of Modern Power Systems and Clean Energy*, vol. 11, no. 1, pp. 267-279, Jan. 2023.

[3] H. Zhang, W. Xiang, W. Lin *et al*., "Grid forming converters in renewable energy sources dominated power grid: control strategy, stability, application, and challenges," *Journal of Modern Power Systems and Clean Energy*, vol. 9, no. 6, pp. 1239-1256, Nov. 2021.

[4] R. Pan, G. Tang, S. Liu *et al*., "Impedance analysis of grid forming control based modular multilevel converters," *Journal of Modern Power Systems and Clean Energy*, vol. 11, no. 3, pp. 967-979, May 2023.

[5] D. Chen, Y. Xu, and A. Huang, "Integration of DC microgrids as virtual synchronous machines into the AC grid," *IEEE Transactions on Industrial Electronics*, vol. 64, no. 9, pp. 7455-7466, Sept. 2017.

[6] G. Li, F. Ma, Y. Wang *et al*., "Design and operation analysis of virtual synchronous compensator," *IEEE Journal of Emerging and Selected Topics in Power Electronics*, vol. 8, no. 4, pp. 3835-3845, Dec. 2020.

[7] L. Huang, H. Xin, and Z. Wang, "Damping low-frequency oscillations through VSC-HVDC stations operated as virtual synchronous machines," *IEEE Transactions on Power Electronics*, vol. 34, no. 6, pp. 5803-5818, Jun. 2019.

[8] J. Liu, Y. Miura, H. Bevrani *et al*., "Enhanced virtual synchronous generator control for parallel inverters in microgrids," *IEEE Transactions on Smart Grid*, vol. 8, no. 5, pp. 2268-2277, Sept. 2017.

[9] Q. Fu, W. Du, and H. Wang. "Influence of multi virtual synchronous generators on power system electromechanical oscillation mode" *Proceedings of the CSEE*, vol. 38, no. 19, pp. 5615-5624, Aug. 2018.

[10] Z. Yang, M. Zhan, D. Liu *et al*., "Small-signal synchronous stability of a new-generation power system with 100% renewable energy," *IEEE Transactions on Power Systems*, vol. 38, no. 5, pp. 4269-4280, Sept. 2023.

[11] H. Liu, D. Sun, P. Song *et al*., "Influence of virtual synchronous generators on low frequency oscillations," *CSEE Journal of Power and Energy Systems*, vol. 8, no. 4, pp. 1029-1038, Jul. 2022.

[12] Y. Yu, S. K. Chaudhary, G. D. A. Tinajero *et al*., "Active damping for dynamic improvement of multiple grid-tied virtual synchronous generators," *IEEE Transactions on Industrial Electronics*, vol. 71, no. 4, pp. 3673-3683, Apr. 2024.

[13] S. D'Arco, J. A. Suul, and O. B. Fosso, "A virtual synchronous machine implementation for distributed control of power converters in smart grids," *Electric Power Systems Research*, vol. 122, pp. 180-197, May 2015.

[14] W. Du, W. Dong, Y. Wang *et al*., "Small-disturbance stability of a wind farm with virtual synchronous generators under the condition of weak grid connection," *IEEE Transactions on Power Systems*, vol. 36, no. 6, pp. 5500-5511, Nov. 2021.

[15] T. Qu, Y. Li, X. Yuan *et al*., "Damping torque coefficient analysis of PMSG-based WT with VSG control considering wind turbine dynamics," *IET Generation*, *Transmission & Distribution*, vol. 17, no. 2, pp. 367-379, Jan. 2023.

[16] Q. Lu, S. Zhao, Y. Yang *et al.*, "Damping torque coefficient analysis of virtual synchronous direct-driven permanent magnetic synchronous generator considering wind turbine dynamics" *High Voltage Engineering*, vol. 48, no. 10, pp. 3838-3847, Feb. 2022.

[17] Z. Wang, K. Zhuang, H. Xin *et al.*, "Low-frequency oscillation mechanism analysis and damping compensation control of virtual synchronous direct-driven wind turbine generators," *Automation of Electric Power Systems*, vol. 48, no. 2, pp. 95-104, Jan. 2024.

[18] L. Chen, X. Du, B. Hu *et al*., "Drivetrain oscillation analysis of grid forming type-IV wind turbine," *IEEE Transactions on Energy Conversion*, vol. 37, no. 4, pp. 2321-2337, Dec. 2022.

[19] W. Du, X. Chen, and H. Wang, "PLL-induced modal resonance of grid-connected PMSGs with the power system electromechanical oscillation modes," *IEEE Transactions on Sustainable Energy*, vol. 8, no. 4, pp. 1581-1591, Oct. 2017.

[20] X. Chen, W. Du, and H. Wang. "Analysis on wide-range-frequency oscillations of power systems integrated with PMSGs under the condition of open-loop modal resonance" *Proceedings of the CSEE*, vol. 39, no. 9, pp. 2625-2635, May 2019.

[21] W. Du, X. Chen, and H. F. Wang, "Power system electromechanical oscillation modes as affected by dynamic interactions from grid-connected PMSGs for wind power generation," *IEEE Transactions on Sustainable Energy*, vol. 8, no. 3, pp. 1301-1312, Jul. 2017.

[22] O. Alizadeh and A. Yazdani, "A control strategy for power regulation in a direct-drive WECS with flexible drive-train," *IEEE Transactions on Sustainable Energy*, vol. 5, no. 4, pp. 1156-1165, Oct. 2014.

[23] S. Alepuz, A. Calle, S. Busquets-Monge *et al*., "Use of stored energy in PMSG rotor inertia for low-voltage ride-through in back-to-back NPC converter-based wind power systems," *IEEE Transactions on Industrial Electronics*, vol. 60, no. 5, pp. 1787-1796, May 2013.

[24] P. S. Kundur, *Power System Stability and Control*. New York: McGraw-Hill Education, 1994.

[25] N. Yang, Q. Liu, and J. D. McCalley, "TCSC controller design for damping interarea oscillations," *IEEE Transactions on Power Systems*, vol. 13, no. 4, pp. 1304-1310, Nov. 1998.

Yizhuo Ma received the B.S. degree in water conservancy and hydropower engineering from Northwest A&F University, Yangling, China, in 2019, and the M.E. degree in water conservancy engineering from Huazhong University of Science and Technology, Wuhan, China, in 2021. He is currently pursuing the Ph.D. degree in electrical engineering at Shanghai Jiao Tong University, Shanghai, China. His research interests include power system stability analysis and control considering wind power integration.

Jin Xu received the B.S. degree in electrical engineering from Sichuan University, Chengdu, China, in 2013, and the Ph.D. degree from Shanghai Jiao Tong University, Shanghai, China, in 2019. He is currently an Assistant Professor at Shanghai Jiao Tong University. His research interests include power system stability analysis, power electronic modeling, and real-time simulation.

Chenxiang Gao received the B. S. and Master degrees from North China Electric Power University, Beijing, China, in 2019 and 2022, respectively. Currently, he is working towards the Ph. D. degree in Shanghai Jiao Tong University, Shanghai, China. His research interests include electromagnetic transient (EMT) equivalent modeling, real-time simulation, and power system stability analysis.

Guojie Li received the B. Eng. and M. E. degrees in electrical engineering from Tsinghua University, Beijing, China, in 1989 and 1993, respectively, and the Ph. D. degree in electrical engineering from Nanyang Technological University, Singapore, in 1999. He was an Associate Professor with the Department of Electrical Engineering, Tsinghua University. He is currently a Professor with the Department of Electrical Engineering, Shanghai Jiaotong University, Shanghai, China. His research interests include power system analysis and control, wind and photovoltaic (PV) power control and integration, and microgrid.

Keyou Wang received the B. S. and M. S. degrees in electrical engineering from Shanghai Jiao Tong University, Shanghai, China, in 2001 and 2004, respectively, and the Ph. D. degree from the Missouri S&T, Springfield, USA, in 2008. He is currently a Professor and Vice Department Chair of Electrical Engineering at Shanghai Jiao Tong University. His research interests include power system dynamic and stability, renewable energy integration, and converter dominated power systems.